Metal-Dependent Interplay between Crystallization and Phosphorus Diffusion during the Synthesis of Metal Phosphide Nanoparticles

S. Carenco, Y. Hu, I. Florea, O. Ersen, C. Boissiere, N. Mezailles, C. Sanchez

Metal-Dependent Interplay between Crystallization and Phosphorus Diffusion during the Synthesis of Metal Phosphide Nanoparticles

S. Carenco,[†,‡] Y. Hu,[‡] I. Florea,[§] O. Ersen,[§] C. Boissière,[†] N. Mézailles,*[,‡,∥] and C. Sanchez*[,†]

[†]Laboratoire de Chimie de la Matière Condensée, Collège de France, UPMC, CNRS, Paris, France

[‡]Laboratoire Hétéroéléments et Coordination, Ecole Polytechnique, CNRS, Palaiseau, France

[§] Institut de Physique et Chimie des Matériaux de Strasbourg, UMR 7504 CNRS—Université de Strasbourg, 23 rue du Loess, 67034 Strasbourg, France

ABSTRACT: The interplay between crystallization and phosphorus diffusion in the versatile synthesis of metal phosphide nanoparticles from well-defined metal nanoparticles is studied by using a favorable "P(0)" source for mechanistic studies: white phosphorus. In this study, the reaction of Ni, Fe, Pd, and Cu nanoparticles with P_4 was quantitative even at relatively low temperatures thanks to the high reactivity of this soluble "P" source. Intermediate amorphous alloys could be identified for the first time in the case of Fe and Pd, while the quantitative character of the reaction provided a selective and controlled access to Pd_5P_4 versus PdP_2 and Cu_3P versus CuP_2. Morphological evolution of the nanoparticles with temperature and M/P stoichiometry was also discussed and provided new insights in the kinetics of the reaction in each case. Hollow Ni2P and FeP nanoparticles were finally obtained while the particularly high stability of the amorphous plain Pd3P nanoparticles was uncovered.

KEYWORDS: *metal phosphide, nanoparticles, morphology control, phase control, white phosphorus*

1. INTRODUCTION

Metal phosphide nanoparticles (M_xP_y) are emerging as a promising class of nanomaterials. Their properties in magnetism,[1] optics,[2] energy storage,[3−6] and catalysis,[7−9] differ significantly from those of the corresponding metal nanoparticles. In the field of catalysis, the phosphide moiety can also tune the catalytic activity and selectivity of the native metal. For example, Ni_2P was found to be particularly suitable for ultradeep hydrodesulfurization, a major challenge of the petroleum industry, because it combines a high activity with an excellent resistance to sulfur poisoning.[10−15] The selectivity of hydrogenation reactions was also found to be controlled by the phosphorus loading in metal-based Ni−P, Co−P, and Mo−P nanocatalysts, either amorphous or crystalline.[16−19]

During the last 20 years, several synthetic routes have been designed for the preparation of metal phosphide nanoparticles well-defined in size, shape, composition, and surface coverage: decomposition of single-source precursors in solution or by CVD,[20,21] decomposition of various aryl- or alkyl-phosphines in the presence of a metal precursor,[22−26] hydrothermal,[27] solvothermal,[28,29] solid-state route using white or red phosphorus.[30] Out of these methods, a most popular has emerged in the past few years, which relies on the decomposition of a high-boiling point alkyl phosphine, tri-*n*-octylphosphine (TOP).[28,31,32] Aside from InP and Cd_3P_2 nanoparticles that are most successfully prepared using $P(SiMe_3)_3$,[33,34] a wide variety of metal phosphide nanoparticles have been obtained, among which are Ni_2P, FeP, CoP, and Pd_5P_2. However, in this method, the TOP is introduced in a large excess and decomposes following unknown reaction pathways. Even though a couple of dedicated mechanistic studies of the nanoscale reaction mechanism appeared very recently in the case of Co−P[35] and Cu−P,[36] rationalization is generally very difficult to make because of the numerous parameters to be taken into account, such as harsh reaction conditions employed, complexity of the procedure (multistep heating, hot injections, syringe-controlled injections), and, last but not least, the nonstoichiometric character of these syntheses. Yields are often not reported, neither for the metal precursor reduction/decomposition nor for the phosphine decomposition. Moreover, the decomposition of TOP requires the use of fairly high temperatures (at least 260 °C), which hampers mechanistic analysis of the amorphization/crystallization events in the nanoparticles during the reaction.

For all these reasons, we have been developing the use of a cheap and much more reactive phosphorus source, white

phosphorus (P_4) as a molecular species in solution, the stoichiometry of which can be, in principle, varied at will. We have shown in a previous work that the reaction of P_4 with nickel(0) species (organometallic Ni complex or preformed nanoparticles) can be easily followed by ^{31}P liquid NMR spectroscopy and that it yielded Ni_2P nanoparticles when used in a 2:1 (Ni/P) ratio.[37] Further extension of this route to In, Pb, and Zn nanoparticles led to InP, Pb_2P, and Zn_3P_2 when using the appropriate M/P ratios.[38] The required temperature was generally much lower than when using TOP, because the P−P bond in the P_4 molecule is quite easy to break compared with the P−C bond of alkylphosphines. In most of the cases, the reaction even started at room temperature. Thus, we could unravel the detailed mechanistic features of the reaction of P_4 with well-defined 25 nm Ni nanoparticles.[39,40] Most importantly, the key intermediate in the reaction was the formation of amorphous Ni−P nanoparticles.

Our goals in the present work are manifold. First, we wished to probe the effects of variable M/P ratios on the existence of one or several M_xP_y phases. Second, we aimed at understanding the mechanism(s) of the formation of the different metal phosphides. Several metals were thus chosen to answer these questions: Ni, Pd, Fe, and Cu. Results of these endeavors are presented herein. The present study highlighted the interplay between P diffusion in the metal nanoparticles and the crystallization of the phosphide phase. The balance between these phenomena was found to strongly depend on the metal, resulting in the possibility to isolate an amorphous intermediate or not, and in the possibility to readily obtain several metal phosphide phases in the cases of Cu and Pd.

2. RESULTS

In the following section, metal(0) nanoparticles (M = Ni, Fe, Pd, Cu) were reacted in solution with precise amounts of white phosphorus (P_4) in order to yield metal phosphide nanoparticles (see Scheme1).

Scheme 1. Schematic Route from Metal Nanoparticles to Metal Phosphide Nanoparticles[a]

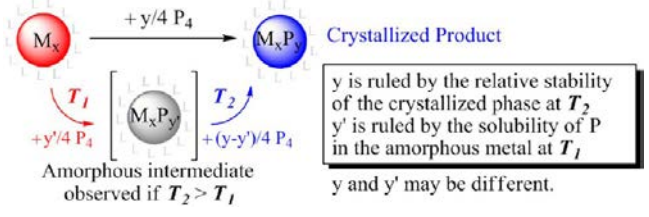

[a] T_1 and T_2 are reaction temperatures. y is the relative amount of phosphorus observed at the end of the reaction in the crystalline nanoparticles, while y' is the relative amount of phosphorus in the intermediate step. Several values for y are possible, and they depend on the metal, according to the M−P phase diagrams. The value of y' is likely to evolve during the course of the reaction, in a range of 0 to the solubility of P in the nanoparticle at the chosen temperature.

Experimental conditions and M/P ratio were investigated to get insights on the reaction mechanism and intermediates. As will be shown, each system exhibited a different behavior related to the following criteria:

(i) Temperature and duration of reaction required to obtain a single product (80 to 320 °C, 30 min to 3 h).

(ii) Formation of an amorphous M_xP_y intermediate prior to the crystallization of the M_xP_y phase (yes/no),

(iii) Possibility to obtain crystallized nanoparticles with several M/P compositions by adjusting the initial M/P stoichiometry (yes/no),

(iv) Morphology of the final metal phosphide nanoparticles (plain, hollow, core−shell, segregated).

A rationale for metal phosphide nanoparticles controlled synthesis is then finally proposed in the last section of this article.

2.1. Nickel. Nickel nanoparticles used in this study were monodispersed 25 nm nanoparticles prepared through a robust and well-understood route.[40] In particular, they were in the fcc phase and made of small 5-nm crystals (see Supporting Information Section 4). Previous studies on the Ni−P system demonstrated that a reaction of these nanoparticles with P_4 at a stoichiometry of Ni/P = 2 lead to crystallized Ni_2P nanoparticles through an amorphous intermediate (Scheme 2). Then, when ratios of Ni/P > 2 were studied, instead of the expected Ni_3P or $Ni_{12}P_5$ phases, an unprecedented phase segregation was observed resulting in the formation of core−shell Ni_2P−Ni nanoparticles. This stands in contrast with recent reports where TOP was used in excess and at higher temperatures as a "P" source to provide the $Ni_{12}P_5$ phase.[41−43] Note that mechanistically, this nanoscaled-induced phase segregation went through a homogeneous and amorphous intermediate (Scheme 2).

In the present study, the Ni−P system was investigated on the P-rich side of the phase diagram (Ni/P < 2) in the hope to obtain different Ni_xP_y phases among which the nanoscaled NiP_2 phase, a phase that is relevant for Li batteries applications.[44] Monodispersed nickel nanoparticles in oleylamine solvent were thus reacted with various amounts of P_4 and the reaction followed by solution ^{31}P NMR spectroscopy, and the resulting solid was analyzed by XRD (X-ray diffraction). Ni/P ratios of 1.3, 1, and 0.5 were tested. In each case, reaction time and temperature were varied. Experimentally, significant amounts of P_4 remained surprisingly unreacted in a broad range of reaction conditions (Figure 1 and Supporting Information Figure 1) as the singlet at −521 ppm for free P_4 was detected by NMR even after a 2 h of heating at 220 °C.

At 90 °C, only an amorphous phase was observed, whereas only Ni_2P crystalline phase started to appear at 150 °C. This Ni_2P phase was fully crystallized at 220 °C, and despite long heating time at this temperature, no other phase formed. No change in the behavior was seen up to 280 °C, but in the case of Ni/P = 0.5, traces of a Ni_5P_4 crystalline phase appeared at 320 °C (for 2 h) (Figure 1).

Selected TEM (transmission electron microscopy) pictures of the resulting nanoparticles are shown in Figure 2. Most interestingly, holes in the nanoparticles are clearly observed for samples obtained from reactions carried out at 220 °C. This is a new feature since the same reaction conducted with a Ni/P ratio of 2 did lead to plain nanoparticles.[39] Thus, the excess of phosphorus seemed to favor the outward diffusion of Ni atom, a fact that may be correlated with a change in surface energy and/or reaction kinetics.

Stronger reaction conditions (320 °C) triggered a deeper morphologic transformation (Figure 2, bottom). Not only were the nanoparticles hollow but they started to deaggregate. At this stage, it should be reminded that the starting 25-nm Ni nanoparticles were made by aggregation of smaller 5-nm nuclei,

Scheme 2. Main Steps of the Reaction of Monodispersed 25 nm Nickel Nanoparticles and P_4 in Solution, Depending on the Ni/P Ratio

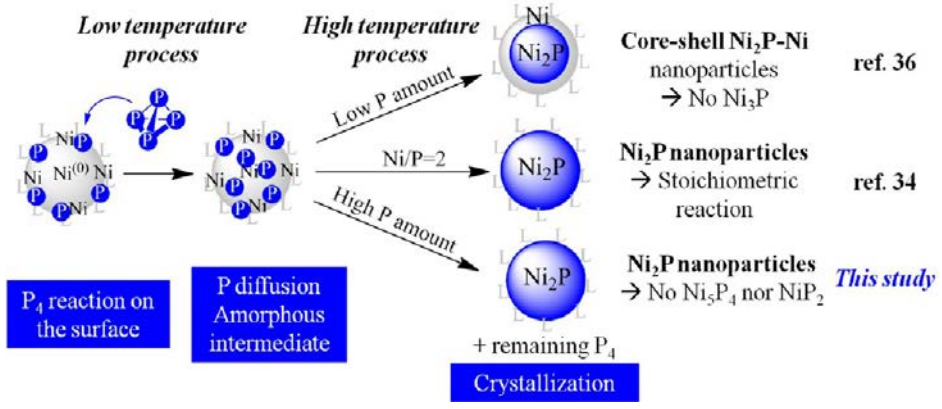

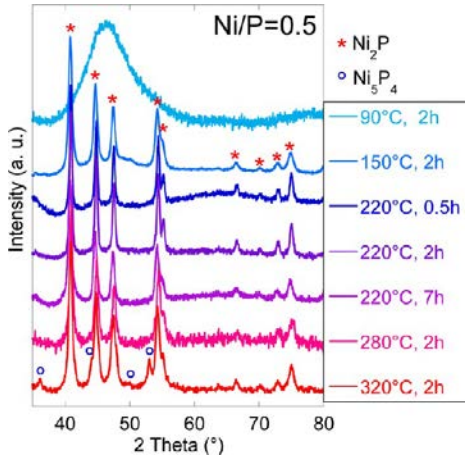

Figure 1. XRD pattern of nickel nanoparticles reacted in solution with P_4 with a stoichiometry of Ni/P = 0.5, for selected conditions of time and temperature. Each pattern was recorded on a different sample.

as shown in a previous mechanistic study, with the nuclei being connected by very thin amorphous nickel (grain boundaries).[40] The faster reaction kinetics imposed by high-temperature conditions seemingly provoked the deaggregation of the nuclei, suggesting that the grain boundaries reacted faster with P_4 than with the crystallized domains. Grain boundaries thus offered a favored diffusion pathway for the P atoms in the Ni nanoparticles.

Altogether, the Ni−P system presented here highlighted two features: (a) it confirmed the existence of a favored phase Ni_2P at the nanoscale, either at low or large Ni/P ratio, and (b) it showed the role of grain boundaries in the P atom diffusion.

2.2. Iron. Prior to the study of the reaction of P_4 with Fe nanoparticles, a reliable synthesis of such nanoparticles had to be chosen. A robust synthesis was selected in the literature,[45] using $Fe(CO)_5$, a commercial Fe(0) source, as the precursor. While this precursor generally yields very monodispersed nanoparticles,[46−49] the reaction is usually not completely quantitative and its yield is difficult to predict, notably because several stable decomposition products such as $Fe_2(CO)_9$ or $Fe_3(CO)_{12}$ are thermally stable.

Nevertheless, monodisperse Fe nanoparticles were synthesized according to Peng et al. and used without isolation to prevent oxidation.[47] Very briefly, $Fe(CO)_5$ was injected in a hot solution (180 °C) of 1-octadecene, containing oleylamine. The temperature was kept at 180 °C for 20 min, then it was cooled, yielding a black solution of ca. 10 nm amorphous Fe(0) nanoparticles (see the Experimental Section and Supporting Information Section 4). It should be noted that the reaction temperature is higher than the boiling point of the precursor (103 °C), requiring the use of a hot-injection procedure. The P_4 stoichiometry was subsequently calculated assuming a quantitative yield (Lacroix et al. reported an isolated yield of 90% for a very similar synthesis),[48] leading to a slight but reasonable overevaluation of the P_4 amount in the following step.

The synthesis of the FeP nanoparticles was investigated first: $^1/_4$ equiv P_4 in toluene was directly added in the flask, toluene was evaporated, and the solution was heated (Scheme 3).

Upon heating at 180 °C, amorphous nanoparticles were obtained (see Supporting Information Figure 5). Nevertheless, a significant amount of the P_4 introduced had reacted with the iron nanoparticles. This reaction was corroborated with the fact that the resulting nanoparticles did not oxidize to Fe_3O_4 upon air exposure during the cleaning procedure. Heating at higher temperature, 250 °C, for 1 h was necessary to obtain the expected crystalline FeP nanoparticles, as shown by XRD (Figure 3, left). It is to be noted that this method allows crystallization at much lower temperature than previously reported.[50]

TEM pictures showed an unexpected morphology of the nanoparticles (Figure 3 right). These nanoparticles appeared to have a 4-nm thick shell with a highly contrasted dark shell and a very poorly contrasted light-gray core, suggesting a hollow structure. Such morphology was not observed for the amorphous nanoparticles synthesized at 180 °C, which are plain (see Supporting Information Figure 5).[51] The hollow structure presumably results from the simultaneous diffusion of phosphorus atoms (inward) and iron atoms (outward) during the reaction, also known as the "nanoscaled Kirkendall effect".[52] These contrasted features observed between reactions carried out at 180 and 250 °C showed that the kinetics of crystallization and atoms migration are similar at 250 °C. Note that the crystalline FeP phase was stable upon limited air exposure, as was the amorphous phase obtained at lower temperature.

Another iron phosphide phase is known at the nanoscale Fe_2P, the formation of which is reported to be competitive with that of FeP. Its formation depends strongly on the reaction conditions.[50] However, no study could use a stoichiometric "P"

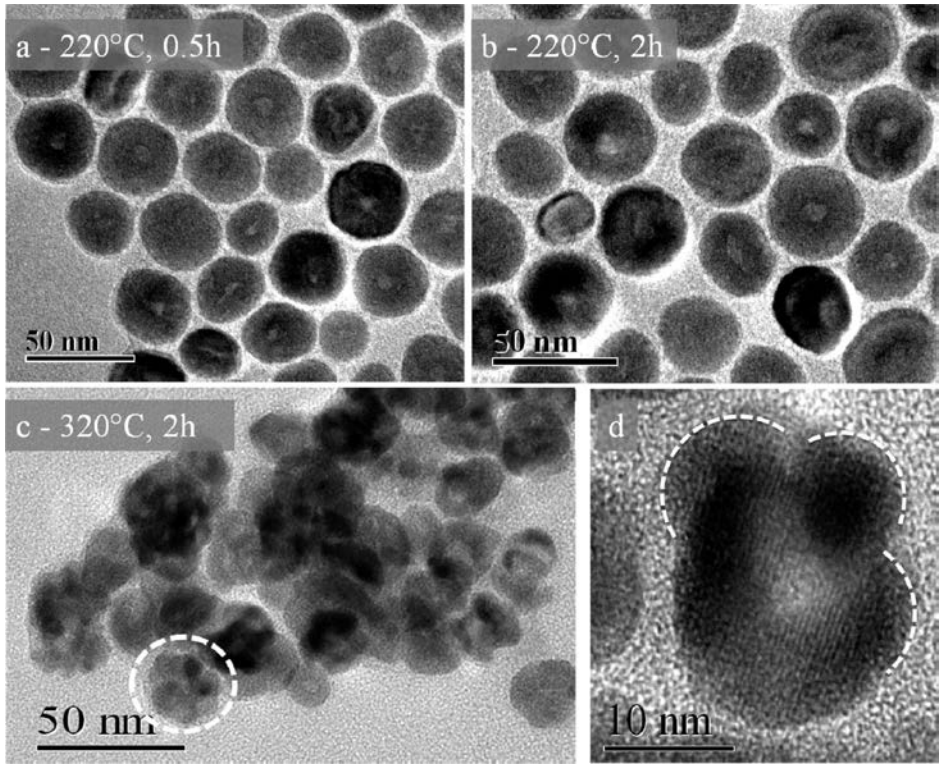

Figure 2. TEM observations of nanoparticles prepared with Ni/P = 0.5, (a) at 220 °C for 0.5 h, (b) at 220 °C for 2 h, and (c) at 320 °C for 2 h. (d) Zoom on the nanoparticle circled in c (the dashed lines are a guide to the eye).

Scheme 3. Synthesis of FeP Nanoparticles

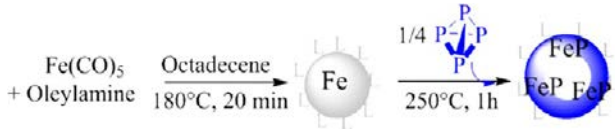

atom donor so far, and our strategy using stoichiometric amounts of P_4 appeared therefore ideal to test the possibility of getting a direct phase-control.

As-made Fe(0) nanoparticles were then reacted with $^1/_8P_4$ at the same temperatures as before: 180 or 250 °C. As in the Fe/P = 1 case, the 180 °C sample was amorphous. To our surprise, the 250 °C sample only exhibited the FeP phase with a hollow morphology (see Supporting Information Figure 6), similar to the one presented above. Note here that the ^{31}P NMR spectrum did not show the presence of remaining nonreacted P_4. Since the introduced stoichiometry was Fe/P = 2, the nanoparticles had to present some amorphous P-poor domains in addition with crystallized FeP ones.

Other ratios of Fe/P were thus tested in order to favor the synthesis of phosphorus-poor phases (Fe_2P or Fe_3P). For the ratio Fe/P = 4, the reaction mixture was heated at 250 °C for 1 h and XRD analysis showed the presence of an amorphous compound, as attested by the broad signal between 40 and 50° (see Supporting Information Figure 7). Most satisfyingly, however, the most intense diffraction peak of the Fe_2P phase could be observed at 40.5°. TEM observation of this material revealed that the nanoparticles had a double-shell structure: an outer shell with a low contrast and an inner shell more

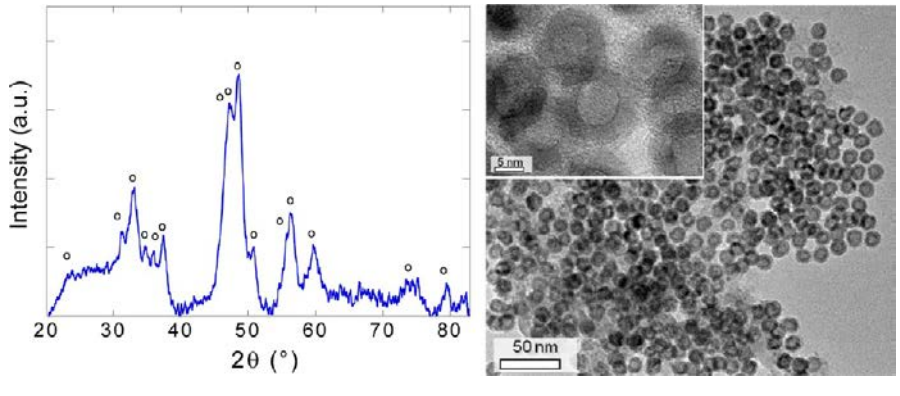

Figure 3. Left: XRD on FeP nanoparticles prepared by heating at 250 °C for 1 h. Circles correspond to the FeP phase. (The broad signal from 20 to 40° corresponds to the glass sample-holder.) Right: TEM observation of crystalline FeP nanoparticles obtained at 250 °C (inset: zoom on a few nanoparticles).

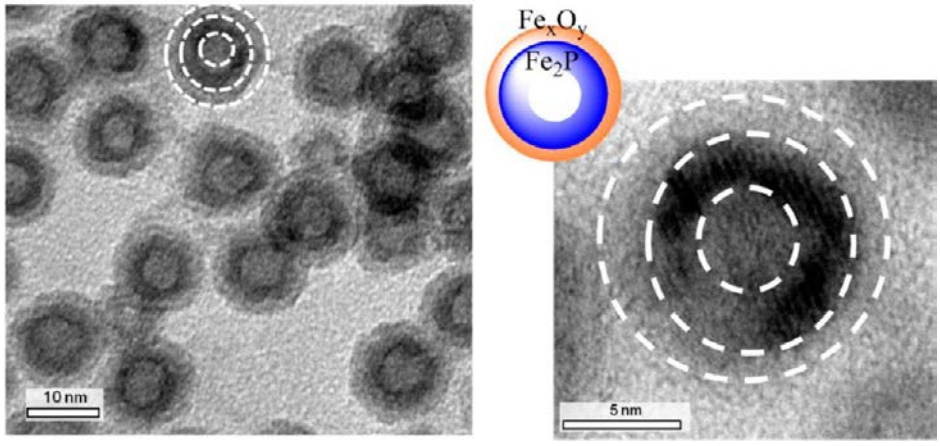

Figure 4. TEM analysis of the nanoparticles prepared with Fe/P = 4 (250 °C, 1h). The pictures showed a three-stage structure, interpreted as a hollow–Fe_2P–Fe_xO_y structure (from inside to outside).

contrasted (Figure 4), while the core was very poorly contrasted and likely hollow. As in the case of nickel,[39] the use of substoichiometric amounts of P_4 apparently triggered a phase segregation inside each nanoparticle.

The outer shell was likely composed of amorphous iron oxide materials, which appeared less contrasted than metal or metal phosphide due to longer Fe–Fe distances. Since the synthesis was carried out in strict air- and water-free conditions, and since the solvent and ligand did not contain oxygen atoms, this oxide shell most likely resulted from an oxidation due to air exposure during the isolation process (Scheme 4). Alternatively, this morphology could also come from a direct oxidation of a unique Fe_2P shell, although Fe_2P has not been reported to be very sensitive to oxidation so far. Moreover, it could still contain phosphorus to some extent, and the outer shell could contain phosphate species.

Scheme 4. Proposed Mechanism for the Formation of the Double-Shell Nanoparticles

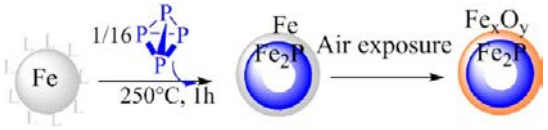

Overall, the use of P_4 as stoichiometric P atom donor showed that FeP is the preferred phase of the iron–phosphorus system. Monodispersed hollow FeP nanoparticles were obtained in stoichiometric conditions and at a relatively low temperature of 250 °C, through a sequence of P insertion followed by crystallization and outward Fe migration. Nevertheless, the Fe_2P phase could be formed in constrained double-shell structures and in substoichiometric amounts of P_4.

2.3. Palladium. The case of palladium showed more versatility, as both a P rich and a P poor crystalline phase could be obtained using stoichiometric amounts of P_4: PdP_2 and Pd_5P_2. They were obtained by reacting the exact required amount of P_4 ($^1/_2$ equiv of P_4 for PdP_2 and $^1/_{10}$ for Pd_5P_2) on Pd nanoparticles synthesized in oleylamine. These nanoparticles were crystallized in the fcc phase (see Supporting Information Section 4). It must be noted that the synthesis was conducted in the absence of trioctylphosphine as a ligand to avoid its further decomposition upon heating. The solution was heated to 310 °C for 2 h, producing single-phase crystalline nanoparticles in a controllable fashion, as observed from XRD patterns (Figure 5). At a lower temperature of 250 °C, the nanoparticles are Pd–P amorphous compounds.

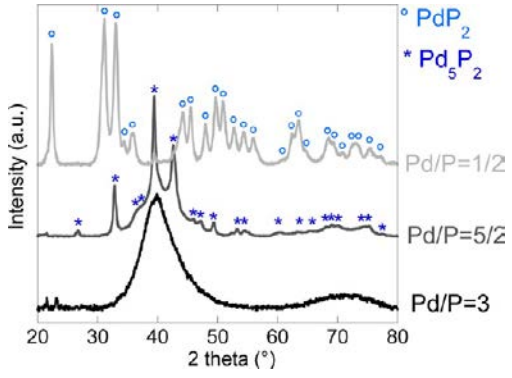

Figure 5. XRD pattern of nanoparticles obtained by reacting P_4 with Pd nanoparticles at 310 °C for 2 h.

Very interestingly, nanoparticles with a lower P content (Pd/P = 3) would not crystallize to the Pd_3P phase at this already quite high temperature (Figure 5, lower pattern). This showed a strong relationship between the composition and the crystallization behavior, all other parameters being identical. The Pd/P = 3 composition clearly provided a species that was less prone to undergo crystallization.[53]

TEM observations of the resulting nanoparticles are presented in Figure 6. The starting 5–7 nm oval Pd nanoparticles (Figure 6a) underwent partial aggregation during the reaction: final nanoparticles were larger (5–20 nm) and presented irregular shapes, resulting from the aggregation of oval shapes. No facet could be observed for the crystallized Pd_5P_2 and PdP_2 nanoparticles (Figure 6c and d), suggesting that the overall surface energy was low compared with the lattice energy.

Altogether, the Pd–P system showed the possibility to obtain selectively two different crystallized phases at the nanoscale. Moreover, it highlighted a deep relationship between composition and crystallization behavior: at 310 °C, the Pd_5P_2 and PdP_2 phases underwent crystallization from amorphous intermediates, while the amorphous Pd_3P would not crystallize.

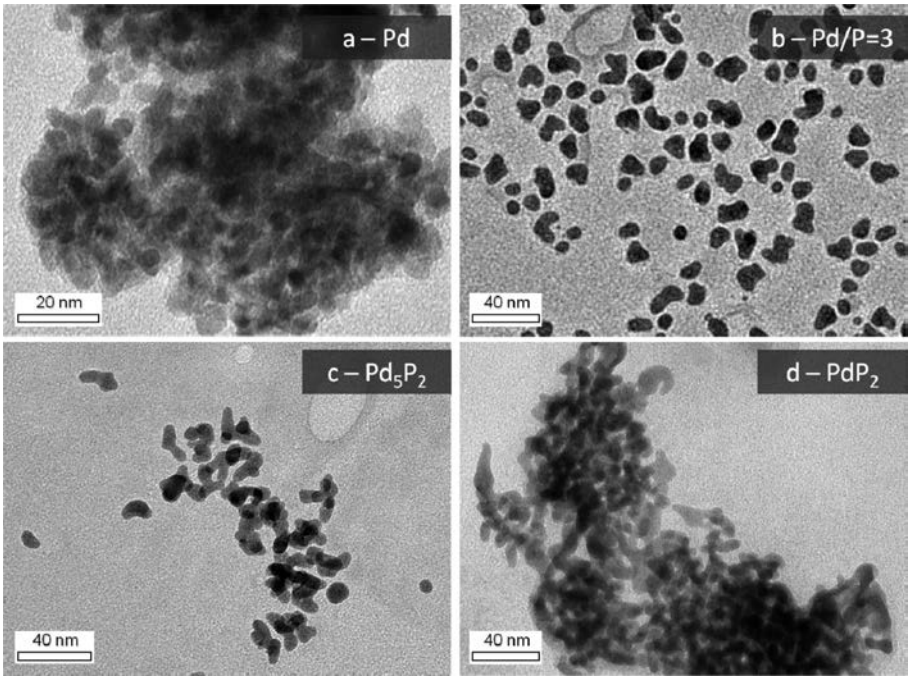

Figure 6. TEM observation of nanoparticles obtained by reacting P_4 with Pd nanoparticles at 310 °C for 2 h. (a) Starting 5–7 nm oval Pd nanoparticles. (b) Amorphous nanoparticles obtained with Pd/P = 3. (c) Crystallized Pd_5P_2 nanoparticles obtained with Pd/P = 2.5. (d) Crystallized PdP_2 nanoparticles obtained with Pd/P = 0.5.

2.4. Copper. The Cu–P system also provided a controlled access to several Cu–P nanoscaled phases. The P-poor Cu_3P and the P-rich CuP_2 nanoparticles could be obtained selectively, using the corresponding stoichiometric amounts of P_4 ($^1/_{12}$ equiv for Cu_3P and $^1/_2$ equiv for CuP_2), as explained below.

Cu nanoparticles were prepared by quantitatively reducing $Cu(acac)_2$ with oleylamine (see the Experimental Section). They were crystallized in the fcc phase (see the Experimental Section and Supporting Information Section 4). Then, the reaction of Cu nanoparticles with $^1/_{12}P_4$ was attempted at 220 °C, a temperature similar to the nickel case. As shown in Figure 7a, Cu_3P nanoparticles were obtained but Cu impurities were still present, which will be discussed later. A slight rise in temperature to 250 °C provided phase pure Cu_3P nanoparticles (Figure 7b and Figure 8.2), which were found to be larger than the initial Cu nanoparticles (Figure 8.1). This pointed out the existence of rearrangements by aggregation and/or by ripening.

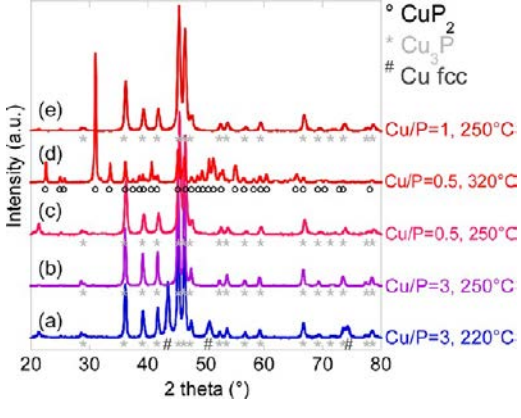

Figure 7. XRD patterns of nanoparticles produced by the reaction of chosen amounts of P_4 on Cu nanoparticles at various temperatures (heating time: 2 h). Crystallite size was estimated to ca 15 nm using the Scherrer formula.

At this temperature, an increased stoichiometry of P_4 (Cu/P = 1 or Cu/P = 0.5) did not result in the formation of phosphorus-rich phases such as Cu_5P_4 or CuP_2. Rather, Cu_3P nanoparticles were formed in both cases (Figure 7e and c, respectively) and the excess P_4 remained unreacted in the solution (it could be observed in the supernatant by a characteristic singlet at −541 ppm in ^{31}P NMR). The nanoparticles morphology was similar to those of the previous Cu_3P sample (Figure 8.3 and 8.4).

The synthesis of phase-pure CuP_2 nanoparticles was finally achieved at a higher temperature of 320 °C, using a stoichiometric ratio of Cu/P = 0.5 (Figure 7d). However, this resulted in a strong aggregation of the nanoparticle inorganic cores, as shown in Figure 8.5. The nanoparticles size increased to several hundred of nanometers for the larger ones. Additionally, the aggregated nanoparticles were found to have aligned crystallization planes, as shown on the right of Figure 8.5. This suggested that the crystallization of the CuP_2 phase occurred after the cores had started to aggregate.

This fact was corroborated by a control reaction. Preformed Cu_3P crystallized nanoparticles were reacted with $^5/_{12}P_4$ (that is, the missing P_4 to go to a Cu/P = 0.5 ratio). The conditions chosen for this reaction were identical to those yielding pure CuP_2 nanoparticles directly from Cu nanoparticles: 2 h of heating at 320 °C. When starting from Cu_3P nanoparticles, the CuP_2 phase was only partially formed and most of the sample still exhibited the Cu_3P phase at the end of the reaction (see Supporting Information Figure 9). Accordingly, the nanoparticles were found to be much less aggregated than in the direct pathway. Altogether, these two experiments showed that Cu_3P was less prone to aggregate than Cu nanoparticles and that the crystallization of CuP_2 is much easier from a

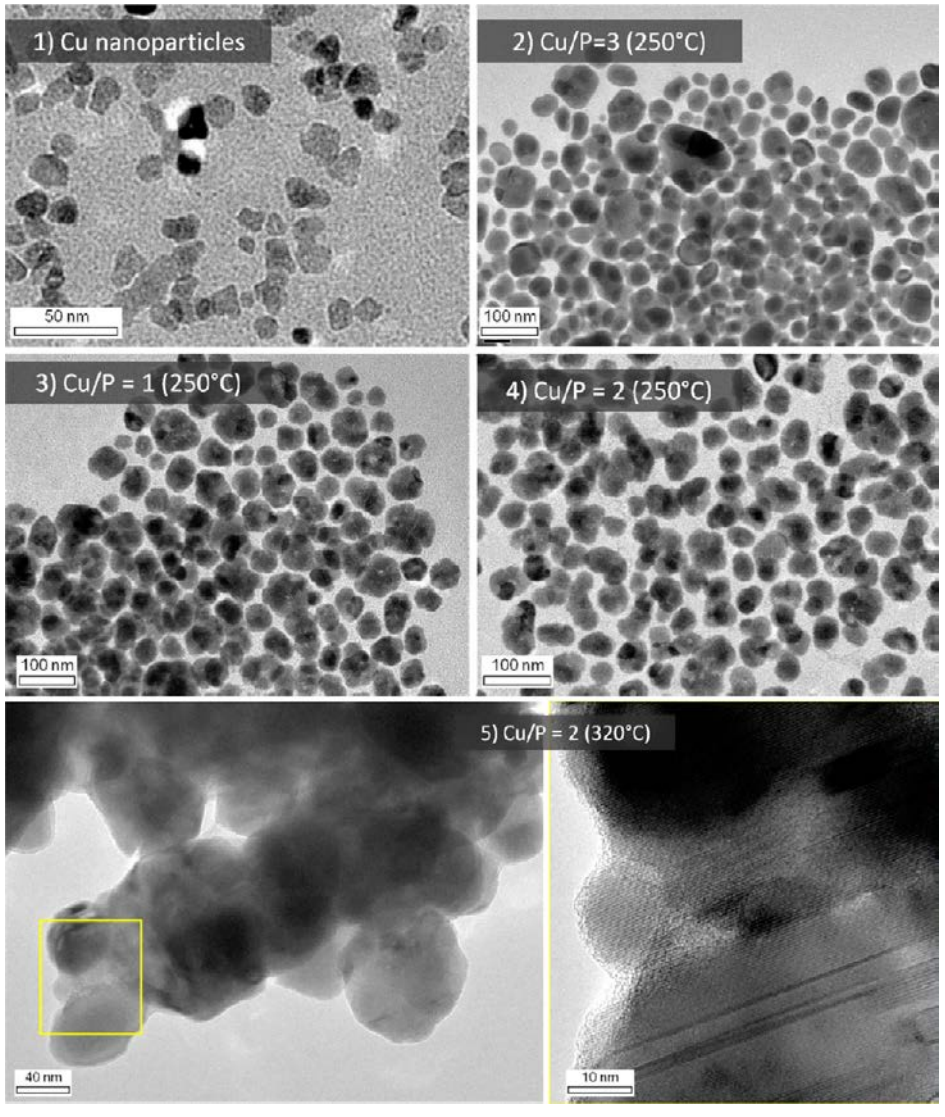

Figure 8. TEM observation of starting Cu nanoparticles (1) and Cu−P nanoparticles synthesized at 250 °C with various Cu/P ratios (2−4). (5) CuP_2 nanoparticles synthesized at 320 °C: Left: overview. Right: HRTEM image of a selected region (interlattice distance is 5.35 Å and corresponds to the (100) orientation). Heating time was 2 h for all samples.

noncrystalline intermediate species than from a crystallized Cu_3P phase.

As noted above, the Cu/P = 3 sample prepared in relatively mild conditions (220 °C for 2 h) did not exhibit the presence of amorphous region but rather a mixture of crystallized Cu and Cu_3P (Figure 7a). This suggested that even though all the P_4 in solution had not yet reacted with the starting Cu nanoparticles, amorphous Cu−P nanoparticles were less favored than a mixture of crystallized compounds. This stood in opposition with observations done for Ni−P, Fe−P, and Pd−P and thus needed further clarification.

The previous synthetic conditions were then adjusted to disfavor the crystallization of Cu_3P; namely, as before, a Cu/P = 3 ratio was employed but the solution was heated only at 100 °C for 30 min. However, even in these very mild conditions, no broad signal corresponding to poorly crystallized Cu−P could be detected by XRD. Rather, a mixture of Cu and Cu_3P was formed (Figure 9 left).

To localize both phases in the sample, advanced high resolution TEM (HRTEM), energy filtered TEM (EFTEM), scanning TEM electron energy loss spectroscopy (STEM-EELS) , and STEM high angle annular dark field (STEM-HAADF) analyses were performed on the nanoparticles. The classical HRTEM images taken on several nanoparticles showed the presence of a thin oxide shell at the surface of the nanoparticles (Supporting Information Figure 10). To confirm this observation, additional measurements were performed using the EFTEM imaging mode,[54,55] which provides 2D elemental maps in a nanomaterial at nanometer scale. By considering as elements of interest the oxygen, the phosphorus, and the copper, these analyses confirmed the presence of an amorphous oxide thin shell at the surface of the nanoparticles (Supporting Information Figure 11). This shell very likely formed upon air exposure. However, it is worth noting here that the comparative analysis of Cu and P chemical maps did not allow to precisely solve the internal composition of the nanoparticles, because of a low signal-to-noise ratio in the P map.

The next approach was to consider the STEM-HAADF imaging, a Z contrast mode well appropriate for a chemical qualitative analysis of specimens.[56] Indeed, these observations showed the presence of a typical core−shell structure (Figure 9,

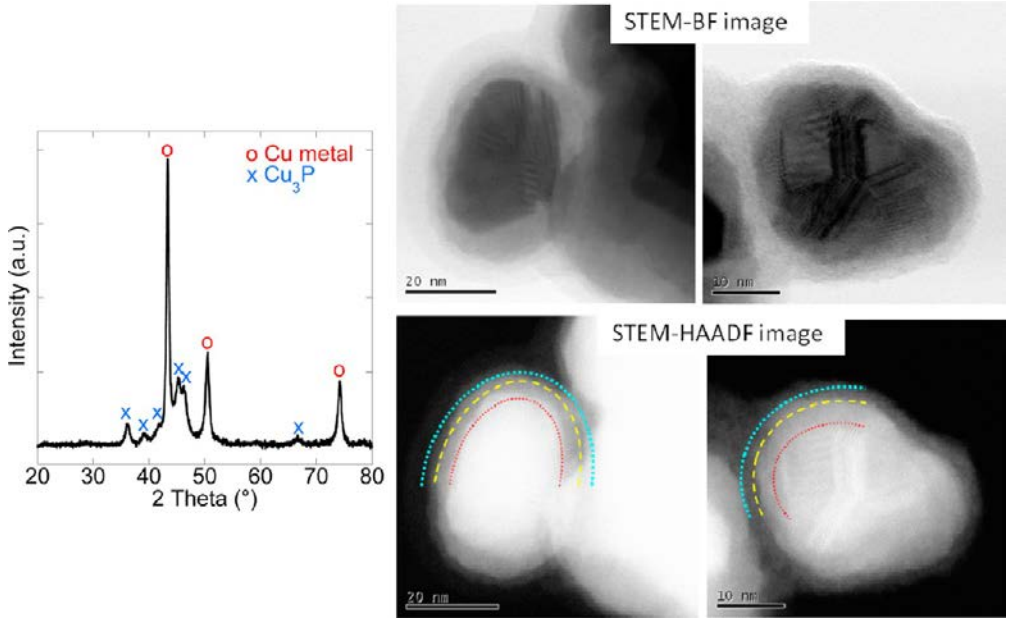

Figure 9. Left: XRD pattern of nanoparticles synthesized with Cu/P = 3 and a mild heating at 100 °C for 30 min. Right: STEM-BF and STEM-HAADF observations on two different nanoparticles synthesized in soft conditions (100 °C for 30 min). The dashes lines are a guide to the eye to localize the $Cu/Cu_3P/Cu_xO$ core/shell/shell structure.

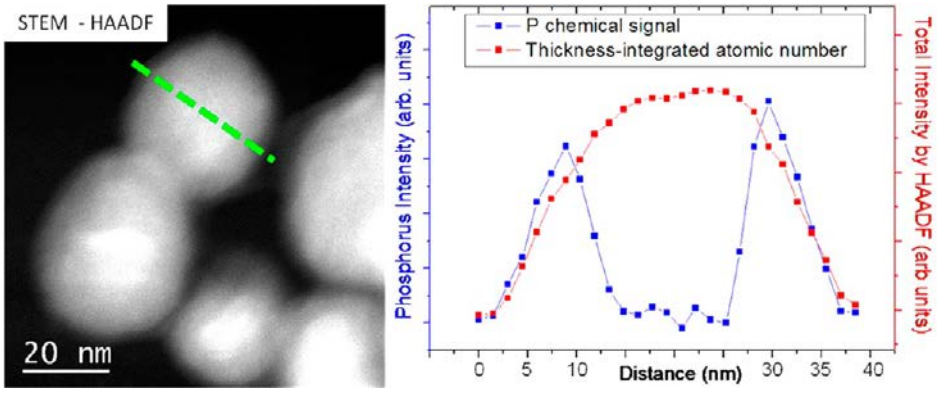

Figure 10. EELS analysis on a typical nanoparticle. Left: STEM-HAADF image showing the scan direction of the electron beam (in green) for the recording of the successive EELS spectra. Right: mass-sensitive intensity (in red) and phosphorus relative concentration (in blue) deduced from the EELS spectra over a cross-section of a nanoparticle synthesized in soft conditions (100 °C for 30 min).

right). More precisely, under the thin external oxide shell (between yellow and blue lines), the nanoparticles were composed of two components: a core more contrasted (inside of red line), and a shell less contrasted (between red and yellow lines). On the same figure, the complementary STEM bright-field images suggested a large crystallite size for the core, while the shell appeared polycrystallized. Finally, analytical measurements in the STEM-EELS mode confirmed the inhomogeneous distribution of P inside the nanoparticles. Several EELS spectra were recorded for various positions of the electron beam focused probe (0.25 nm in diameter). Figure 10 presents the dark-field image of one of the analyzed nanoparticles on which the electron beam was moved on the line schematized in green nanoparticles. The relative concentration of phosphorus was measured using small probes areas (2.5 nm in size) and was plotted in Figure 10 (see Figure 12 of Supporting Information for a typical EELS spectrum showing the L_{23}-edge of phosphorus.). It showed unambiguously that the P amount is higher in the vicinity of the nanoparticle surface, finally confirming the architecture of the internal structure of nanoparticles: a core composed of Cu, with the shell below the thin oxide layer containing phosphorus and composed of copper phosphide. These findings are in agreement with the results of XRD (Figure 9, left), which showed that the domains attributed to metallic Cu were larger than the Cu_3P ones (thinner peaks for Cu indicating a crystallite size of ca 12 nm, broader peaks for Cu_3P indicating a crystallite size of ca 4 nm).

Moreover, further HRTEM observations confirmed this structure. In particular, some of the larger nanoparticles of the sample could even present two cores of Cu surrounded by Cu_3P (Supporting Information Figure 13).

The detailed structural analysis and the very soft conditions used for the synthesis of these nanoparticles allowed concluding on the reaction mechanism (Scheme 5). The Cu nanoparticles reacted incompletely with P_4 due to the low temperature (100 °C) and short time used (30 min). As a result, the remaining P_4 could be observed in the solution by ^{31}P NMR. However, instead of producing amorphous nanoparticles such as in the

Scheme 5. Mechanism for the Formation of the Double-Shell $Cu/Cu_3P/Cu_xO$ Nanoparticles

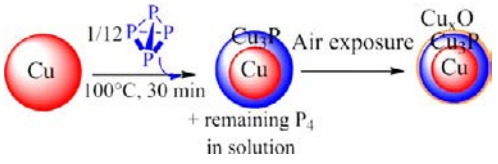

case of nickel, palladium, or iron, the crystallization of Cu_3P was observed. Upon air exposure during the washing of the nanoparticles, a thin layer of copper oxide formed on the very external surface of the nanoparticles.

Very interestingly, the Cu−P system exhibited a strong tendency to crystallization, compared with the other systems discussed. The crystallization of Cu_3P was observed in very mild condition and led to an original core−shell $Cu-Cu_3P$ structure. It must be noted that this structure is different from the Janus structure recently obtained in much stronger conditions (350 °C) by De Trizio et al.,[57] using the tri-*n*-octylphosphine as a phosphorus donor. This highlighted that, in very soft conditions, the core−shell structure can be stabilized.

3. DISCUSSION

In this study, different behaviors were uncovered when reacting a metal nanoparticle with controlled amounts of P_4 (Scheme 6). It should be reminded at this stage that the solvent, ligand, and reaction conditions were systematically selected to preclude the formation of metal oxide in the course of the reaction: a thin layer of metal oxide was formed for the most air-sensitive metals (Fe and Cu) only in the latter cleaning steps at room temperature and thus do not explain the various behavior observed. Moreover, the possible influence of ligands on the morphology of the nanoparticles will not be discussed here, as we tried to use mainly oleylamine as a surface ligand (and also TOP in the Ni−P system), but one should keep in mind that its interaction with the surface might be fairly different from one metal to another.

In the case of nickel, the Ni_2P phase that had been shown to be particularly stable when using substoichiometric amounts of P_4 is confirmed in its status on the other side of the phase diagram (for Ni/P < 2) at temperatures up to 320 °C. However, at such high temperatures, the kinetics of diffusion was found to be modified by the larger amounts of P and resulted in the outward diffusion of Ni in the course of the reaction. This produced hollow nanoparticles.

In the case of iron, the formation of crystallized FeP hollow nanoparticles was observed when heating amorphous non-hollow FeP nanoparticles at 250 °C. Interestingly, the Fe_2P phase could not be obtained by using the corresponding theoretical stoichiometry (Fe/P = 2). Rather, nonpure Fe_2P hollow double-shell nanoparticles were formed when using even less phosphorus (Fe/P = 4). This suggested that FeP is a preferred phase at this scale, but that Fe_2P may be obtained from an amorphous Fe−P intermediate in P-poor systems.

The palladium system provided a richer pallet of crystallized nanoscaled compounds since both Pd_5P_2 and PdP_2 could be obtained selectively, using the theoretical Pd/P ratio. However, high reaction temperature was required to crystallize the nanoparticles, highlighting the relative stability of Pd−P amorphous nanoparticles. This fact was corroborated with the oval shape morphology of these nanoparticles, which suggested low surface energy and no propensity for the particles to yield faceted, crystallized structures. Very interestingly, Pd_3P nanoparticles were found to be extremely stable as an amorphous species and would not crystallize even at elevated temperatures (320 °C).

The copper system, on the opposite, demonstrated no propensity to stabilize amorphous species. Even at very low temperature (100 °C) and with nonquantitative reaction of P_4 on Cu nanoparticles, only crystallized species were identified: the Cu core of the nanoparticles remained unreacted while the shell, accessible through a shorter diffusion length, reacted with

Scheme 6. Overview of the Reaction Pathways Identified in This Study and of the Most Relevant Parameters for Each System

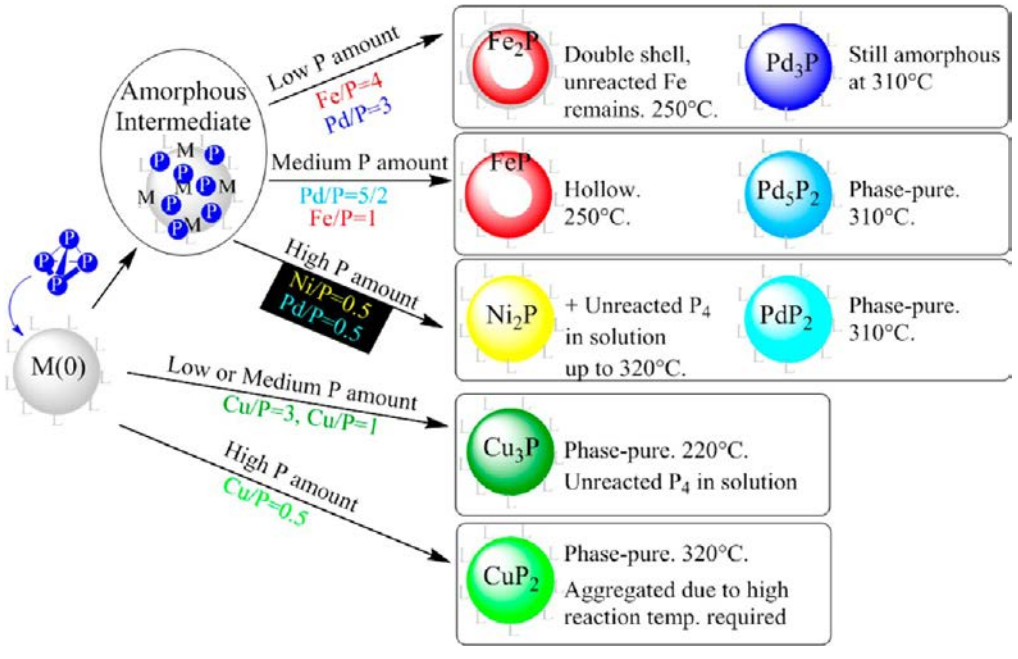

P_4 and readily produced Cu_3P crystallites. A rise in temperature allowed to complete the reaction and yielded phase pure Cu_3P. Phase-pure CuP_2 could also be obtained selectively from Cu nanoparticles, but the required reaction temperature was found to be higher (320 °C), since only the Cu_3P phase would form at the intermediate temperature of 250 °C. Resulting CuP_2 nanoparticles morphology was found to be profoundly different than the one of the starting nanoparticles. Aggregation occurred in the course of the reaction and before the crystallization of the CuP_2 species.

Interestingly, these four late-transition metal thus exhibited very different behaviors that could not be reconciled in a single mechanism, as of today. The temperatures T_1 and T_2 discussed in Scheme 1 were found to be in the order $T_1 < T_2$, except for Cu. The Pd system suggested a strong dependence of the M/P final ratio (y value of Scheme 1) and the crystallization temperature T_2, a phenomenon that will be explored in detail in a further report. Diffusion kinetics was suggested to be responsible for the various morphology observed but aggregation phenomena could not be neglected either at the higher reaction temperatures (>250 °C). The cross-talk between diffusion and crystallization also likely relies on other parameters such as (i) the surface tension (or the interfacial energy) of the metal versus the phosphide, (ii) the existence of lattice defects in the nanoparticles, (iii) the enthalpic gain associated with the formation of M−P bonds. Measuring *in operando* the evolution of the value of y' (ideally, with spatial and time resolution) will be of major importance, since all these parameters are a function of both the temperature and the composition.

In conclusion, this study pertaining to the accessibility of different phases of the M_xP_y system at the nanoscale could be conducted in conditions that were unprecedented in this topic: a perfect control of the "P atom" stoichiometry, because of the use of P_4, a highly reactive "P" source. It unraveled the strong interplay between the metal choice and the metal phosphides crystallization pathway. As a consequence, an in depth understanding of each metal phosphide synthesis was provided, both concerning the possibility to obtain selectively several M_xP_y phases and the rationale for the reaction temperature required for crystallization. In summary,

(i) nickel nanoparticles were found to yield preferentially Ni_2P nanoparticles even in a large excess of phosphorus,
(ii) iron nanoparticles yielded preferentially FeP nanoparticles although poorly crystallized Fe_2P could be observed in substoichiometric conditions,
(iii) palladium nanoparticles could yield both Pd_5P_2 and PdP_2 nanoparticles by changing the P_4 stoichiometry, though high temperatures were required for crystallization of the phases,
(iv) copper nanoparticles could yield Cu_3P nanoparticles but no amorphous intermediate could be observed.

This model study on nanoscale transformation from metal to metal phosphides also lays the foundations for a new methodological approach in nonoxides nanoparticles synthesis (borides, carbides, nitrides, sulfides), based on the use of a highly reactive heteroelement source (here, P_4) to develop a full understanding of thermodynamics and kinetics of such transformations at the nanoscale.

4. EXPERIMENTAL SECTION

Oleylamine (OA, Aldrich, 70%) and 1-octadecene (ODE, Aldrich, 90%) were used as received. Dry $Ni(acac)_2$ was obtained from $Ni(acac)_2$ hydrate (Strem) by a Dean−Stark distillation in toluene under nitrogen and stored in the glovebox. Trioctylphosphine (TOP), $Pd(acac)_2$, $Cu(acac)_2$, and $Fe(CO)_5$ were purchased from Strem and used as received. White phosphorus was taken from the laboratory's own chemical stockroom, where it was regularly stored under water. It was dried under inert conditions, washed with degassed THF and dissolved in toluene to produce stock solution of known concentration (measured by ^{31}P NMR, in the range 0.1−0.4 mol/L).

Safety note: White phosphorus is stable in water but highly flammable and toxic if swallowed or inhaled. It is incompatible with strong oxidizing agents and strong bases. It is light and heat sensitive. It should be handled accordingly.

Experimental Procedures. All reactions were carried out under nitrogen atmosphere using standard air-free techniques. After cooling the reaction to room temperature (r.t.), the centrifugation steps were done under air.

Nickel Nanoparticles. Ni nanoparticles were prepared from dry $Ni(acac)_2$, according to ref 40, using 0.8 equiv of TOP and 2 h of heating at 220 °C. The nanoparticles were not isolated before the second step. An aliquot was taken for TEM and XRD characterization.

Ni−P Nanoparticles. Attempts to produce NiP_2 nanoparticles were conducted as follows: The nickel nanoparticles (3.90 mmol of Ni) were reacted on P_4 (solution in toluene) as described in ref 39, using a higher stoichiometry of P_4 (Ni/P = 0.5). The heating conditions were varied from 90 to 320 °C, for 0.5 to 7 h, as described in Figure 1. The nanoparticles were collected by centrifugation and the supernatant was analyzed by ^{31}P solution NMR.

Iron. Fe nanoparticles were prepared according to ref 46, using 5.2 mmol of $Fe(CO)_5$ (1 equiv) as a starting material. The nanoparticles were not isolated before the second step. An aliquot was taken for TEM and XRD characterization.

Fe−P Nanoparticles. FeP nanoparticles were prepared by adding P_4 (5.6 mmol of P, 1 equiv P). The toluene was evaporated under vacuum. The solution was heated under inert atmosphere to 250 °C for 2 h using a heating mantle. The solution was cooled, and the nanoparticles were isolated by addition of acetone (30 mL) and centrifugation.

Palladium. In a typical experiment, oleylamine (8 equiv, 0.788 mmol, 210 mg) and 1-octadecene (4 mL) were introduced in a Schlenk tube and degassed under vacuum. $Pd(acac)_2$ (1 equiv, 0.0985 mmol, 30 mg) was then added to the solution. The mixture was heated to the desired temperature (180 °C) using an oil bath. After 2 h of heating, the solution was cooled to r.t. The resulting solution of Pd(0) nanoparticles was used as such for the second step (addition of P_4). For analysis purposes, they were washed by redispersion in THF (4 mL), acetone (30 mL) was added, and the mixture was centrifuged. This washing process was repeated three times. The nanoparticles were not isolated before the second step. An aliquot was taken for TEM and XRD characterization.

Pd−P Nanoparticles. To the as-synthesized Pd(0) mixture, the required amount of P_4 in solution in toluene was added: $^1/_2$ equiv of P_4 for PdP_2 ($4.92.10^{-2}$ mmol), $^1/_{10}$ for Pd_5P_2 ($9.85.10^{-3}$ mmol), and $^1/_{12}$ for Pd_3P ($8.20.10^{-3}$ mmol). The mixture was stirred at the required temperature (310 °C) for 2 h. After cooling to r.t., the nanoparticles were collected by centrifugation. They were washed by redispersion in THF (4 mL), acetone (30 mL) was added, and they were centrifuged. This washing process was repeated three times.

Copper Nanoparticles. Cu nanoparticles were prepared by reducing $Cu(acac)_2$ with oleylamine in a fashion similar to that of the Ni nanoparticles. $Cu(acac)_2$ (0.764 mmol, 1 equiv) was added to a degassed oleylamine (7.64 mmol, 10 equiv) in ODE (6 mL) in a 100 mL flask. The solution was heated to 250 °C for 2 h, using a heating mantle, and then cooled to room temperature. The nanoparticles were not isolated before the next step. An aliquot was taken for TEM and XRD characterization.

Cu–P Nanoparticles. Cu_3P nanoparticles were obtained by reacting the Cu nanoparticles with P_4 (0.255 mmol, 0.33 equiv of P). The toluene was evaporated under vacuum. The solution was heated under inert atmosphere to 220 °C for 2 h using a heating mantle. The solution was cooled and the nanoparticles were isolated by addition of acetone (30 mL) and centrifugation. CuP_2 nanoparticles were obtained in a similar fashion, by increasing the P_4 amount to 0.5 equiv (in P_4) and adjusting the heating temperature to 320 °C.

Characterizations. Powder XRD measurements were performed with a Bruker D8 X-ray diffractometer operating in the reflection mode at Cu Kα radiation with 40 kV beam voltage and 40 mA beam current. The data were collected in the 20–80° range (2α) with steps of 0.05° and a counting time of at least 2 s.

^{31}P Liquid Nuclear Magnetic Resonance (NMR). NMR spectra were recorded on a Bruker AMX-300 spectrometer. ^{31}P chemical shifts are relative to a 85% H_3PO_4 external reference. P_4 was detected as a singlet at −521 ppm.

Transmission Electron Microscopy (TEM). For routine analysis, samples were prepared by evaporating a drop of hexanes diluted suspension of the nanoparticles on a carbon-coated copper grid. The nanoparticles were studied using a TECNAI 120 (120 kV) apparatus.

The TEM analysis on the Cu_3P–Cu nanocomposite were done using a Jeol 2100F (FEG) TEM/STEM electron microscope operating at 200 kV, equipped with a TRIDIEM post-column imaging filter of the Gatan Company. The samples were dispersed in ethanol in an ultrasonic bath for a few minutes. The solution was then deposited on a copper grid covered by a holey carbon membrane.

EFTEM–STEM–HAADF. To obtain 2D elemental maps for O, P, and Cu on the nanoparticles, EFTEM images have been recorded using the three-windows method on the K edge of O (532 eV), L_{23} edge of P (132 eV), and L_{23} edge of Cu (920 eV)

The STEM-EELS spectra were recorded for various positions of the electron beam focused probe (0.25 nm in diameter) using a convergent angle α of about 25 mrad and a collection angle β of 30 mrad. The recording of the EELS spectra on the P–L_{23} edge was performed using DigiScan in combination with Spectrum Imaging (SI), both plug-in Digital Micrograph software. The total spectrum was obtained by averaging 70 EELS SI spectra with 2 s exposure time using a 2 mm spectrometer aperture and a dispersion of 0.3 eV/channel.

ASSOCIATED CONTENT

Supporting Information

Additional data for the Ni–P system, the Fe–system, the Cu–P system, and the metal nanoparticles. This material is available free of charge via the Internet at http://pubs.acs.org.

AUTHOR INFORMATION

Corresponding Author

E-mail: mezailles@chimie.ups-tlse.fr; clement.sanchez@college-de-france.fr.

Present Address

[‖]Laboratoire "Hétérochimie Fondamentale et Appliquée", Université Paul Sabatier, CNRS, 31062 Toulouse, France

Notes

The authors declare no competing financial interest.

ACKNOWLEDGMENTS

The authors acknowledge financial support from the CNRS (FR3507) and CEA METSA network. The CNRS, the Collège de France, the Ecole Polytechnique, and the UPMC are also acknowledged for financial support. S.C. acknowledges the DGA for financial support.

REFERENCES

(1) Brock, S. L.; Perera, S. C.; Stamm, K. L. *Chem.—Eur. J.* **2004**, *10*, 3364–71.
(2) Xie, R.; Battaglia, D.; Peng, X. *J. Am. Chem. Soc.* **2007**, *129*, 15432–3.
(3) Souza, D. C. S.; Pralong, V.; Jacobson, A. J.; Nazar, L. F. *Science* **2002**, *296*, 2012–5.
(4) Gillot, F.; Boyanov, S.; Dupont, L.; Doublet, M.-L.; Morcrette, M.; Monconduit, L.; Tarascon, J.-M. *Chem. Mater.* **2005**, *17*, 6327–6337.
(5) Cabana, J.; Monconduit, L.; Larcher, D.; Palacín, M. R. *Adv. Mater.* **2010**, *22*, E170–92.
(6) Carenco, S.; Surcin, C.; Morcrette, M.; Larcher, D.; Mézailles, N.; Boissière, C.; Sanchez, C. *Chem. Mater.* **2012**, *24*, 688–697.
(7) Alexander, A.-M.; Hargreaves, J. S. J. *Chem. Soc. Rev.* **2010**, *39*, 4388–401.
(8) Senevirathne, K.; Burns, A. W.; Bussell, M. E.; Brock, S. L. *Adv. Funct. Mater.* **2007**, *17*, 3933–3939.
(9) Carenco, S.; Leyva-Pérez, A.; Concepción, P.; Boissière, C.; Mézailles, N.; Sanchez, C.; Corma, A. *Nano Today* **2012**, *7*, 21–28.
(10) Oyama, S. T.; Gott, T.; Zhao, H.; Lee, Y.-K. *Catal. Today* **2009**, *143*, 94–107.
(11) Yang, S.; Liang, C.; Prins, R. *J. Catal.* **2006**, *237*, 118–130.
(12) Fuks, D.; Vingurt, D.; Landau, M. V.; Herskowitz, M. *J. Phys. Chem. C* **2010**, *114*, 13313–13321.
(13) Wang, R.; Smith, K. J. *Applied Catal., A* **2009**, *361*, 18–25.
(14) Duan, X.; Teng, Y.; Wang, A.; Kogan, V.; Li, X.; Wang, Y. *J. Catal.* **2009**, *261*, 232–240.
(15) Nelson, A.; Sun, M.; Junaid, A. *J. Catal.* **2006**, *241*, 180–188.
(16) Deng, J.-F.; Li, H.; Wang, W. *Catal. Today* **1999**, *51*, 113–125.
(17) Li, H.; Dai, W. L.; Wang, W.; Fang, Z.; Deng, J. F. *Appl. Surf. Sci.* **1999**, *152*, 25–34.
(18) Yang, P.; Jiang, Z.; Ying, P.; Li, C. *J. Catal.* **2008**, *253*, 66–73.
(19) Li, X.; Zhang, Y.; Wang, A.; Wang, Y.; Hu, Y. *Catal. Commun.* **2010**, *11*, 1129–1132.
(20) Panneerselvam, A.; Malik, M. a; Afzaal, M.; O'Brien, P.; Helliwell, M. *J. Am. Chem. Soc.* **2008**, *130*, 2420–1.
(21) Liu, C.; Dai, L.; You, L. P.; Xu, W. J.; Ma, R. M.; Yang, W. Q.; Zhang, Y. F.; Qin, G. G. *J. Mater. Chem.* **2008**, *18*, 3912.
(22) George, P. P.; Pol, V. G.; Gedanken, A. *J. Nanoparticle Res.* **2007**, *9*, 1187–1193.
(23) Sweet, J. D.; Casadonte, D. J. *Ultrason. Sonochem.* **2001**, *8*, 97–101.
(24) Zheng, X.; Yuan, S.; Tian, Z.; Yin, S.; He, J.; Liu, K.; Liu, L. *Mater. Lett.* **2009**, *63*, 2283–2285.
(25) Kelly, A. T.; Rusakova, I.; Ould-Ely, T.; Hofmann, C.; Lüttge, A.; Whitmire, K. H. *Nano Lett.* **2007**, *7*, 2920–5.
(26) Colson, A. C.; Whitmire, K. H. *Chem. Mater.* **2011**, *23*, 3731–3739.
(27) Su, H.; Xie, Y.; Li, B.; Liu, X. M.; Qian, Y. T. *Solid State Ionics* **1999**, *122*, 157–160.
(28) Park, J.-G.; Park, J.; Koo, B.; Yoon, K. Y.; Hwang, Y.; Kang, M.; Hyeon, T. *J. Am. Chem. Soc.* **2005**, *127*, 8433–40.
(29) Zhang, H.; Ha, D.-H.; Hovden, R.; Kourkoutis, L. F.; Robinson, R. D. *Nano Lett.* **2011**, *11*, 188–97.
(30) Barry, B. M.; Gillan, E. G. *Chem. Mater.* **2009**, *21*, 4454–4461.
(31) Qian, C.; Kim, F.; Ma, L.; Tsui, F.; Yang, P.; Liu, J. *J. Am. Chem. Soc.* **2004**, *126*, 1195–8.
(32) Henkes, A. E.; Schaak, R. E. *Chem. Mater.* **2007**, *19*, 4234–4242.
(33) Li, L.; Reiss, P. *J. Am. Chem. Soc.* **2008**, *130*, 11588–9.
(34) Ojo, W.-S.; Xu, S.; Delpech, F.; Nayral, C.; Chaudret, B. *Angew. Chem., Int. Ed.* **2012**, *51*, 738–741.
(35) Ha, D.-H.; Moreau, L. M.; Bealing, C. R.; Zhang, H.; Hennig, R. G.; Robinson, R. D. *J. Mater. Chem.* **2011**, *21*, 11498.
(36) De Trizio, L.; Figuerola, A.; Manna, L.; Genovese, A.; George, C.; Brescia, R.; Saghi, Z.; Simonutti, R.; Van Huis, M.; Falqui, A. *ACS Nano* **2011**, *6*, 32–41.
(37) Carenco, S.; Resa, I.; Le Goff, X.; Le Floch, P.; Mézailles, N. *Chem. Commun.* **2008**, 2568–70.

(38) Carenco, S.; Demange, M.; Shi, J.; Boissière, C.; Sanchez, C.; Le Floch, P.; Mézailles, N. *Chem. Commun.* **2010**, *46*, 5578−80.
(39) Carenco, S.; Le Goff, X. F.; Shi, J.; Roiban, L.; Ersen, O.; Boissière, C.; Sanchez, C.; Mézailles, N. *Chem. Mater.* **2011**, *23*, 2270−2277.
(40) (a) Carenco, S.; Boissière, C.; Nicole, L.; Sanchez, C.; Le Floch, P.; Mézailles, N. *Chem. Mater.* **2010**, *22*, 1340−1349. (b) Carenco, S.; Labouille, S.; Bouchonnet, S.; Boissière, C.; Le Goff, X.-F.; Sanchez, C.; Mézailles, N. *Chem.—Eur. J.* **2012**, DOI: 10.1002/chem.201201071..
(41) Muthuswamy, E.; Savithra, G. H. L.; Brock, S. L. *ACS Nano* **2011**, *5*, 2402−11.
(42) Muthuswamy, E.; Brock, S. L. *Chem. Commun.* **2011**, *47*, 12334−6.
(43) Wang, J.; Johnston-Peck, A. C.; Tracy, J. B. *Chem. Mater.* **2009**, *21*, 4462−4467.
(44) Aso, K.; Hayashi, A.; Tatsumisago, M. *Inorg. Chem.* **2011**, *50*, 10820−4.
(45) Yan, J.-M.; Zhang, X.-B.; Han, S.; Shioyama, H.; Xu, Q. *Angew. Chem., Int. Ed.* **2008**, *47*, 2287. (b) Huber, D. L. *Small* **2005**, *1*, 482. (c) Dumestre, F.; Chaudret, B.; Amiens, C.; Renaud, P.; Fejes, P. *Science* **2004**, *303*, 821. (d) Meffre, A.; Lachaize, S.; Gatel, C.; Respaud, M.; Chaudret, B. *J. Mater. Chem.* **2011**, *21*, 13464. (e) Lacroix, L.-M.; Lachaize, S.; Falqui, A.; Respaud, M.; Chaudret, B. *J. Am. Chem. Soc.* **2009**, *131*, 549. (f) Phua, P.-H.; Lefort, L.; Boogers, J. A. F.; Tristany, M.; de Vries, J. G. *Chem. Commun.* **2009**, 3747. (g) Zhao, Y.; Cui, G.; Wang, J.; Fan, M. *Inorg. Chem.* **2009**, *48*, 10435. (h) Yamamoto, S.; Ruwan, G.; Tamada, Y.; Kohara, K.; Kusano, Y.; Sasano, T.; Ohno, K.; Tsujii, Y.; Kageyama, H.; Ono, T.; Takano, M. *Chem. Mater.* **2011**, *23*, 1564. (i) Cheong, S.; Ferguson, P.; Feindel, K. W.; Hermans, I. F.; Callaghan, P. T.; Meyer, C.; Slocombe, A.; Su, C.-H.; Cheng, F.-Y.; Yeh, C.-S.; Ingham, B.; Toney, M. F.; Tilley, R. D. *Angew. Chem., Int. Ed.* **2011**, *50*, 4206.
(46) Chen, Y.-X.; Chen, S.-P.; Zhou, Z.-Y.; Tian, N.; Jiang, Y.-X.; Sun, S.-G.; Ding, Y.; Wang, Z. L. *J. Am. Chem. Soc.* **2009**, *131*, 10860.
(47) Peng, S.; Wang, C.; Xie, J.; Sun, S. *J. Am. Chem. Soc.* **2006**, *128*, 10676.
(48) Lacroix, L.-M.; Huls, N. F.; Ho, D.; Sun, X.; Cheng, K.; Sun, S. *Nano Lett.* **2011**, *11*, 1641.
(49) Kura, H.; Takahashi, M.; Ogawa, T. *J. Phys. Chem. C* **2010**, *114*, 5835.
(50) See for instance: (a) Muthuswamy, E.; Kharel, P. R.; Lawes, G.; Brock, S. L. *ACS Nano* **2009**, *3*, 2383. (b) Park, J.; Koo, B.; Hwang, Y.; Bae, C.; An, K.; Park, J.-G.; Park, H. M.; Hyeon, T. *Angew. Chem., Int. Ed.* **2004**, *43*, 2282.
(51) By ^{31}P liquid NMR, no P_4 could be detected in the supernatant of the reaction producing amorphous FeP nanoparticles.
(52) See, for instance, (a) Yin, Y.; Rioux, R. M.; Erdonmez, C. K.; Hughes, S.; Somorjai, G. A.; Alivisatos, A. P. *Science* **2004**, *304*, 711. (b) Cabot, A.; Ibáñez, M.; Guardia, P.; Alivisatos, A. P. *J. Am. Chem. Soc.* **2009**, *131*, 11326. (c) Railsback, J. G.; Johnston-Peck, A. C.; Wang, J.; Tracy, J. B. *ACS Nano* **2010**, *4*, 1913. (d) Chiang, R.-K.; Chiang, R.-T. *Inorg. Chem.* **2007**, *46*, 369.
(53) A detailed account will be provided in a separate report.
(54) Florea, I.; Ersen, O.; Hirlimann, C.; Roiban, L.; Deneuve, A.; Houlle, M.; Janowska, I.; Nguyen, P.; Pham, C.; Pham-Huu, C. *Nanoscale* **2010**, *2* (12), 2668−2678.
(55) Roiban, L.; Sorbier, L.; Pichon, C.; Bayle-Guillemaud, P.; Werckmann, J.; Drillon, M.; Ersen, O. *Microsc. Microanal.* **2012**, DOI: 10.1017/S143192761200116X.
(56) Burgin, J.; Florea, I.; Majimel, J.; Dobri, A.; Ersen, O.; Tréguer-Delapierre, M. *Nanoscale* **2012**, *4*, 1299−1303.
(57) De Trizio, L.; Figuerola, A.; Manna, L.; Genovese, A.; George, C.; Brescia, R.; Saghi, Z.; Simonutti, R.; Van Huis, M.; Falqui, A. *ACS Nano* **2012**, *6*, 32−41.